Divergence-Free Correction for Synthetic Wind Fields

Dangi, Nirav; Sodja, Jurij; Yu, Wei

DOI
10.1002/we.70062

Publication date
2025

Document Version
Final published version

Published in
Wind Energy

Wind Energy

WILEY

RESEARCH ARTICLE OPEN ACCESS

Divergence-Free Correction for Synthetic Wind Fields

Nirav Dangi[1] | Jurij Sodja[2] | Wei Yu[1]

[1]Flow Physics and Technology, Aerospace Engineering, Delft University of Technology (TU Delft), Delft, Netherlands | [2]Aerospace Structures and Materials, Aerospace Engineering, Delft University of Technology (TU Delft), Delft, Netherlands

Correspondence: Nirav Dangi (n.s.dangi@tudelft.nl)

Received: 4 May 2025 | **Revised:** 15 September 2025 | **Accepted:** 20 September 2025

Funding: This work was supported by the Korea Institute of Energy Technology Evaluation and Planning (KETEP) grant funded by the Korea Government (MOTIE) (20228520020050).

Keywords: CFD | divergence-free | Poisson | wind turbine loads

ABSTRACT

Synthetic wind fields generated for wind turbine simulations do not satisfy incompressibility condition, thus, are not divergence-free. This results in spurious pressure fluctuations when input as a boundary condition to, for example, incompressible large eddy simulations (LES). This study investigates the impact of divergence-free correction on synthetic wind fields and their influence on wind turbine loads. Although divergence-free correction methods exist, they often modify the wind field energy spectrum and unsteady characteristics. Ongoing research addresses these challenges, but the acceptability of such changes and their impact on wind turbine loads has not been adequately studied. This work enforced incompressibility using the Helmholtz–Hodge decomposition, solved through spectral and spatial methods. An efficient Fourier-based spectral method was implemented, validated, and tested against the traditional finite difference method used for the spatial approach. Synthetic wind fields based on three coherence models were analyzed under three turbine operating conditions. An aeroelastic analysis of the IEA 22 MW wind turbine was performed in the 54 wind fields before and after divergence correction. Spectral analysis revealed a reduction in energy at specific frequencies after the correction for incompressibility. Additionally, the standard deviations of the wind velocities changed (despite similar means), consequently affecting the aeroelastic turbine response. A new iterative correction method is proposed to mitigate these effects, which preserves first- and second-order statistics while enforcing a divergence-free condition. This method is recursively applied, maintaining RMSE changes to the wind field within user-specified bounds. Key findings show that the iterative method yields an excellent match in the longitudinal wind field energy spectrum and a closer match in wind field standard deviation across the rotor, reducing discrepancies in turbine response. Some discrepancies in the lateral and vertical velocity components' higher order statistics were observed. Standard divergence correction (without RMSE constraints) led to a decrease of up to 20% in the tower fore-aft moment, while the proposed method reduces this change to −10%. The tower top side-side moment was found to increase by 20% by using the former approach, while the proposed correction reduced this increase to 10%. Blade root flap-wise bending moment was less affected (up to 5% reduction). Divergence-free wind fields, even with similar statistical properties, influence aeroelastic loads. The proposed method aims to achieve physically consistent and more comparable wind field analyses and resulting wind loads.

1 | Introduction

Turbulence is a complex state of fluid motion, consisting of pseudo-random yet coherent patterns across various spatial and temporal scales, overlaid on an underlying mean flow. The range of motions is continuous between large scales determined by the geometry of the problem and small scales determined by the viscosity of the fluid [1]. Numerous

methodologies can be used to generate turbulence, which can be classified into recycling methods and synthetic methods [1, 2]. The former involves using turbulence modeling and numerical simulations to solve for the fluid flow using the Navier–Stokes equations for a sufficient amount of time to allow for turbulence generation. The latter uses a mathematical procedure to synthesize the turbulence generation to fulfill certain constraints. The fidelity of these synthesized fluctuations to real turbulence determines how the Navier–Stokes equations treat them when used as an inflow boundary condition in incompressible numerical simulations. The reader is referred to [1–4] for a review of these methods and to [5, 6] for a detailed comparison of the performance of different inflow generation methods in simulating the atmospheric boundary layer (ABL). In one such study, the authors in [6] use various synthetic inflow wind fields as an input to computational fluid dynamics (CFD) simulations. They report considerable deviations between target and observed values of the wind field, which emphasizes the need to refine synthetic methods further.

First of all, a brief introduction to the synthetic method is provided. In computational wind engineering, generating synthetic turbulence with defined statistical characteristics is essential for numerous applications [7, 8]. The low computational cost of synthetic methods makes them more practical for problems of industrial interest. The desired characteristics include, but are not limited to, mean-velocity profiles, turbulence spectra, and representative spatial and temporal correlations. This topic has been the focus of extensive research for decades, resulting in the emergence of various methodological approaches. Such wind fields allow for the assessment of wind loads on structures in a controlled and practical manner. Synthesized turbulent wind fields may be generated, for instance, using Fourier techniques [9, 10], digital filtering techniques [11, 12], and synthetic-eddy methods [13]. Within the synthetic methods, this article focuses on the Fourier techniques. It may be noted that the abovementioned synthetic methods may not generally satisfy the continuity equation. In [14], a method was proposed for divergence-free inflow using the Fourier method; however, it was applicable only for homogeneous and isotropic turbulence, which is not truly representative of the ABL [15, 16]. Recent improvements to the Fourier method, which can generate anisotropic turbulence, have been proposed in [2]. Similarly, enhancements to the synthetic-eddy method have been introduced in [17]. However, research on these methods is still not fully mature and needs further development and validation. Aiming in general for more realism in synthetic fields, and ensuring incompressibility, a recent article in [18] proposes a model to generate generalized Gaussian wind fields to what they refer to as superstatistical random fields. Their approach focuses on constraining these random fields on sparse, pointwise atmospheric turbulence measurements to solve the problem of incomplete measurements.

Fourier techniques for generating inflow turbulence are based on decomposing turbulence onto a set of harmonic functions based on Fourier analysis. Typically, the procedure involves using Fourier modes with random phases and a target wind field energy spectrum to generate spatially uncorrelated wind field fluctuations. Next, a coherence function is introduced, and the spatial correlation information is added using Cholesky decomposition [19]. Lastly, the mean wind profile is added to the fluctuations, resulting in a temporally (using target spectra) and spatially (using target coherence function) correlated wind field, albeit with random phases. However, this procedure does not take into account the compatibility of the synthesized wind field with the continuity equation. Consequently, such wind fields may not be divergence-free. Hence, despite excellent spatial and temporal correlation, the wind fields are not directly suitable for use as an input to, for example, numerical simulations using large eddy simulation (LES).

Various studies have tackled this drawback and developed methods for introducing a divergence-free correction to the synthesized wind fields. Several methods involve an a posteriori correction of the synthetic wind field. These research efforts stem from the fact that if the synthetic turbulent wind fields do not satisfy the continuity equation, spurious pressure fluctuations appear in incompressible numerical simulations to enforce a divergence-free wind field, leading to inaccuracy in the wind field and poor convergence of simulations [17, 20–22]. In [20], a method inspired by [23] is used to correct the synthetic wind field for incompressibility. The technique from [24] is a modification of the algorithm suggested by [25], inspired by the well-known pressure-implicit with splitting of operators (PISO) algorithm [26] in CFD simulations. These methods are applied transiently, that is, at every time step of the synthetic wind field or the numerical simulation. In [27], the authors develop a method based on a minimal Lagrangian map to deform a Gaussian field generated using random-phase Fourier modes, and ensuring incompressibility, and to receive a desired spectrum. Another approach is to correct the wind field for incompressibility using the Helmholtz–Hodge decomposition[1]. This approach allows a divergence-free wind field to be used in applications beyond CFD. For example, one may use more realistic wind fields for wind turbine load assessments. The approach can also be utilized for wind farm blockage models, for example, as seen in [33]. The book by [34] describes the Helmholtz–Hodge decomposition as: *Let $\vec{\zeta}$ be a sufficiently smooth vector field on a bounded domain Ω, with a smooth boundary $\partial\Omega$. Then, $\vec{\zeta}$ can be uniquely decomposed in the form: $\vec{\zeta} = \nabla D + \vec{r}$, where D is a scalar potential function, the vector field $\vec{r}$ has zero divergence and is tangential to the boundary along $\partial\Omega$.* Using this information, one may apply the divergence operator to the equation and find that the scalar potential D can be found by solving the Poisson's equation $\nabla^2 D = \nabla \cdot \vec{\zeta}$ and then the incompressible field $\vec{r}$ can be found.[2] Various methods exist to solve Poisson's equation with corresponding boundary conditions (see [30] for different methods specifically for applying the Helmholtz-decomposition theorem). The most often used methods can be considered either the finite difference methods (FDM), which involve solving a system of linear equations with matrix operations, or the Fourier method, which leverages the properties of the Fourier transform to speed up the computation. However, it may be noted that the latter faces challenges related to boundary conditions and signal periodicity, to name a few (see also [35, 36]). In the field of magnetohydrodynamics, the article [37] is also referred to, which discusses divergence-cleaning solvers in the same context.

This introduction emphasizes that the divergence-free correction to synthetic wind fields has gathered significant attention, and continuous efforts are made to make them more realistic.

For example, the method from [24] is used and tested by the authors of [38]. Still, despite similar mean wind profiles in the corrected wind field, considerable changes were observed in the turbulence intensity profiles. Another study that tackles this problem is found in [39], which optimizes the difference in Reynolds stresses from a target value. The main objective of this study is to improve the accuracy of representing the wind field using synthetic methods, for example, when applying synthetic turbulence in numerical simulations or wind load simulations. In line with the literature, this article addresses two key research questions to achieve this goal: (1) How can an algorithm be developed to enforce the divergence-free condition in synthetic wind fields while preserving the characteristics of the original field as closely as possible?

(2) What are the effects of neglecting the divergence-free condition on the aeroelastic response of a large wind turbine rotor?

To address these research questions, an iterative method is proposed in this article to resolve the unacceptable differences in the wind field (as demonstrated later in this study), which fulfills both Taylor's hypothesis and the divergence-free condition in the corrected wind field (both identified as essential in the study by [2]). A total of 54 different wind fields differing in terms of mean wind profiles and coherence models are used in this study for a comprehensive assessment and to reduce bias due to, for example, random seeds. The iterative method is based on solving the Helmholtz–Hodge decomposition using a typical FDM method and an efficient FFT-based approach. Lastly, a comprehensive analysis is conducted on the wind fields and the resulting wind turbine loads in the original and the divergence-free wind field, to demonstrate the improved accuracy of the proposed iterative algorithm. To contextualize this article in the wind energy domain, it can be noted that the current wind turbine design standard laid out in the International Electrotechnical Commission (IEC) [40] document makes use of two spectral methods, the more physical Mann model [41, 42] and the method hereafter referred to as, the Kaimal model, given by the Kaimal auto spectrum [43] with the modified [44] Davenport's exponential coherence model [45]. Theoretically, the homogeneous isotropic Mann model-based wind field with no shear satisfies the incompressibility condition. However, due to the discrete (not continuous) numerical implementation and for anistropic Mann model-based wind fields, this is not the case (for instance, see Figure 6 of [46]). This study uses the synthetic wind field approach with the IEC coherence function and two other coherence functions for a comprehensive analysis.

The structure of this article is as follows: in Section 2, the methods used in this study are explained, namely, the synthetic wind field generation and the Helmholtz–Hodge decomposition implementation. Next, Subsection 2.3 describes the simulated wind fields and the aeroelastic simulation setup. A thorough comparison of the wind field characteristics before and after the iterative correction is presented in Section 3. In Section 4, the impact of the differences in wind fields on the wind turbine aeroelastic response is investigated. Lastly, conclusions and recommendations are discussed in Section 5. The validation of the Poisson solver developed in this study is provided in Appendix A.

2 | Methods

2.1 | Synthetic Wind Fields

This study utilizes a total of 54 distinct wind fields, corresponding to a combination of three hub-height wind speeds for the IEA 22 MW wind turbine [47, 48], three coherence models, and six different random seeds ($3 \times 3 \times 6$). These wind fields differ regarding the inflow conditions, specifically the hub-height wind speed, the coherence model applied, and the stochastic variability introduced through different random seeds. The three hub-height wind speed conditions were set as 8.5 m/s (below-rated), 11.5 m/s (at-rated) and 14.5 m/s (above-rated). The wind shear profile for the synthetic wind fields was set based on neutral atmosphere LES results, described in [49]. The three coherence models selected were the IEC coherence function [40], the Shiotani and Iwatani coherence function (see chapter 9 of [50]), and a modified version of the Shiotani and Iwatani function, hereafter referred to as SHIW0 and SHIW1, respectively. The IEC coherence function for an arbitrary separation r is given by Equation (1) [51, 52].

$$\gamma^2_{\mathrm{IEC}}(r,f) = \left(\exp\left(-12\sqrt{\left(\frac{f\cdot r}{V_{\mathrm{hub}}}\right)^2 + \left(\frac{0.12\cdot r}{L_{c,\mathrm{IEC}}}\right)^2}\right)\right)^2 \tag{1}$$

The IEC coherence γ^2_{IEC} is given in Equation (1), where f is the frequency in Hz, r represents the length of the projection of the vector that separates the two points onto a plane that is perpendicular to the average direction of the wind, L_c is the coherence scale parameter given as $8.1\Lambda_1$ [51], where $\Lambda_1 = 42$ m is the longitudinal turbulence scale parameter, for wind load analysis of wind turbines with hub heights ≥ 60 m, and V_{hub} is the velocity at the hub height.

The SHIW0 coherence function for vertical (z) and lateral (y) directions is given by Equation (2).

$$\begin{aligned} \gamma^2(z,f) &= \exp\left(-a_z f\frac{\Delta z}{V}\right), & \gamma^2(y,f) &= \exp\left(-a_y f\frac{\Delta y}{V}\right), \\ a_z &= 12 + 11\frac{\Delta z}{z}, & a_y &= 28\left(\frac{\Delta y}{z}\right)^{0.45} \end{aligned} \tag{2}$$

In Equation (2), the coherence functions are defined for only purely vertical and lateral points. However, obtaining the coherence functions for diagonally separated points is also necessary. The final interpolated SHIW0 coherence function for an arbitrary separation $r = \sqrt{y^2 + z^2}$ is given by Equation (3).

$$\gamma^2(y,z,f) = \exp\left(-\sqrt{\left(\frac{28\left(\frac{\Delta y}{z}\right)^{0.45} f\Delta y}{V}\right)^2 + \left(\frac{\left(12+11\frac{\Delta z}{z}\right) f\Delta z}{V}\right)^2}\right) \tag{3}$$

It can be noticed that in Equation (1), there is no dependence on altitude (z) and there is no distinction between decay parameters for the lateral and vertical coherence, unlike Equation (3). A modified coherence function, SHIW1, was used in addition to the abovementioned functions. This altered function was treated such that the decay in both lateral and vertical separations was

the same, matching the vertical separation decay of the SHIW0 model, and $a = a_z$ was employed. It may be noted that the objective of using multiple coherence functions was to test the robustness of the proposed algorithm in this study—not to compare the coherence models.

The synthetic wind fields were generated by adapting the open-source code [53], which was used in [54] and demonstrated computational efficiency according to [55]. The synthetic wind fields were generated for 1024s with a time step of 0.25s, leading to a total of 4096 steps. This 2–D plane of wind data was converted to a 3–D wind box using Taylor's frozen turbulence hypothesis [56]. The mean wind speed at hub height and the time step were used to convert time steps into spatial steps, for use in the Helmholtz–Hodge decomposition. Although a widely used approach, it should be noted that the use of mean wind speed at hub height for the time–space conversion implies that the distortional effect of shear is not considered in generating the turbulence box. Given the hub-height wind speeds of 8.5, 11.5, and 14.5m/s, and the time step used in this study, the stream-wise spacing (Δx) was 2.125, 2.875, and 3.625 m, respectively. Given the total duration of 1024s and the different hub-height wind speeds, the spanwise length (L_x) of the wind field after implementing Taylor's hypothesis was 8.704, 11.776, and 14.848km, respectively. The spanwise (Δy) and altitude-wise spacing (Δz) used was 10m with 35 points in each direction. This led to the total elements in the 3–D wind field to be 5017600 elements. A grid sensitivity study was conducted, which highlighted the implemented divergence-correction algorithm's robustness to changes in grid size (see Appendix C).

A mathematical coherence formulation was used to assess the obtained wind field coherence. The cocoherence, quad-coherence, and root coherence were computed (Equation (4), where f is the frequency). These refer to the real part, imaginary part, and amplitude of a 2-point cross-spectrum, respectively, normalized by the product of power spectra for each point [57].

$$\gamma = \underbrace{\frac{\mathrm{Re}\left[S_{xy}(f)\right]}{\sqrt{S_{xx}(f)S_{yy}(f)}}}_{\text{co - coherence}} + \underbrace{\frac{\mathrm{Im}\left[S_{xy}(f)\right]}{\sqrt{S_{xx}(f)S_{yy}(f)}}}_{\text{quad - coherence}} \tag{4}$$

Both the IEC Kaimal and the SHIW coherence model ignore the quad cocoherence. Hence, only the cocoherence will be presented and discussed in this study. All estimates of cocoherence are later provided using the Welch method [58] with seven segments, 50% overlap, and a Hann window function. A simple moving average filter over 5 points smoothed the resulting cocoherence estimates. Lastly, the wind field spatial autocorrelation was assessed, as also done in [20], following which the integral length scales in the stream-wise and spanwise directions were calculated with the formulations described in [59] and shown in Equation (5).

$$\begin{aligned} L_i^x &= \overline{U} \cdot \int_{t=0}^{t(R_i(t)=0)} R_i(t)\mathrm{d}t \\ L_i^y &= \int_0^{+\infty} R_i(\tau), \mathrm{d}\tau \end{aligned} \tag{5}$$

The stream-wise integral length scale is denoted by L_i^x, and the spanwise integral length scale is denoted by L_i^y. Here, i denotes the three wind speed components, R_i is the single-sided autocovariance function of the fluctuating wind velocity, and τ denotes the time lag. L_i^x was computed based on the integration up to the first zero-crossing [60] of R_i. L_i^y was calculated by an integral of an exponential decay function to approximate the correlation coefficients as a function of spanwise separation [59].

2.2 | Helmholtz–Hodge Decomposition

The synthetic wind fields in this study were corrected to enforce incompressibility using the Helmholtz–Hodge decomposition. The Helmholtz–Hodge decomposition allows for decomposition of the wind field ($\bar{\zeta}$) into an irrotational ($\bar{d}$) and an incompressible field ($\bar{r}$). This is shown in Equation (6) [30], where D is a scalar potential.

$$\bar{\zeta} = \nabla D + \bar{r} = \underbrace{\bar{d}}_{\textit{irrotational}} + \underbrace{\bar{r}}_{\textit{incompressible}} \Rightarrow \bar{r} = \bar{\zeta} - \nabla D \tag{6}$$

Since by definition the field $\bar{r}$ is divergence-free ($\nabla \cdot \bar{r} = 0$), taking the divergence of Equation (6) allows one to solve for D and finally find $\bar{r}$. This is shown in Equation (7), where the Laplacian ∇^2 is replaced by $\mathscr{L}$ for brevity.

$$\nabla \cdot \bar{\zeta} = \nabla^2 D + \nabla \cdot \bar{r} \Rightarrow \nabla \cdot \bar{\zeta} = \mathscr{L}(D) \tag{7}$$

Hence, it can be seen that a Poisson's equation needs to be solved with the appropriate boundary conditions to find the scalar potential D. This is typically done using FDM or Fourier methods. As mentioned previously, the several instantaneous wind field values in a 2–D plane were converted to a 3–D domain by means of Taylor's frozen turbulence assumption. Thus, the Poisson equation was solved for the entire wind field at once for both methods. Firstly, the FDM method involves discretizing the equations and solving a system of linear equations typically written as $Ax = b$. Thus, the equation solved is given as Equation (8).

$$\mathscr{L}(D) = \nabla \cdot \bar{\zeta} \Rightarrow M_\zeta D = \nabla \cdot \bar{\zeta} \Rightarrow D = M_\zeta^{-1} \nabla \cdot \bar{\zeta} \tag{8}$$

In Equation (8), the Laplacian was discretized with 1–D Laplacian matrices for Neumann boundary conditions, as shown in Equation (9) (see Chapter 9.4 of [61] and Chapter 4.8.4 of [62]).

$$\begin{aligned} &M_\zeta = \mathrm{diag}(\mathbf{b}) + \mathrm{diag}(\mathbf{j}, 1) + \mathrm{diag}(\mathbf{j}, -1), \mathbf{b} = (-2, \ldots, -2) \in \mathbb{R}^{N_\zeta}, \\ &b_1 = b_{N_\zeta} = -1, \mathbf{j} = (1, \ldots, 1) \in \mathbb{R}^{N_\zeta - 1}, \quad \zeta \in \{x, y, z\} \end{aligned} \tag{9}$$

The final Laplacian matrix was constructed in Equation (10).

$$M_\zeta = \frac{1}{dx^2}\left(I_z \otimes I_y \otimes M_x\right) + \frac{1}{dy^2}\left(I_z \otimes M_y \otimes I_x\right) + \frac{1}{dz^2}\left(M_z \otimes I_y \otimes I_x\right). \tag{10}$$

In Equation (10), the stream-wise, spanwise, and altitude-wise grid spacing is given by dx, dy, and dz, respectively. The operator $\otimes$ is the Kronecker product, and I_x, I_y, and I_z represent sparse

identity matrices. The divergence of the original wind field ($\nabla \cdot \bar{\zeta}$) was input using a fourth-order finite difference scheme. With this discretization, Equation (8) was solved to obtain the scalar potential D. The equation was iteratively solved until the residuals reached a convergence threshold of $\mathcal{O}(10^{-4})$. The validation of the implementation is provided in Appendix A. Finally, the gradient ∇D was found using a fourth-order FDM to solve for the incompressible wind field $\bar{r} = \bar{\zeta} - \nabla D$.

A second method implemented in this study is the Fourier method to solve the Poisson equation in spectral space, which allows for a significant speedup. Once again, the equation to be solved is $\mathscr{L}(D) = \nabla \cdot \bar{\zeta}$. Once again, the divergence of the original wind field ($\nabla \cdot \bar{\zeta}$) was found using a fourth-order finite difference scheme, and the rest of the steps were conducted in the Fourier domain as discussed below. Thus, for brevity, let $\nabla \cdot \bar{\zeta} = \mathcal{G}$. To satisfy the requirements of the Fourier method, $\mathcal{G}$ was checked for periodicity in x and y directions and indicated periodicity to be a reasonable assumption. However, to satisfy a no-flow through condition in the z direction, a mirror extension was applied on the bottom boundary to ensure gradients vanish at z boundaries. This led to an increase in memory overhead, but still lower than the memory overhead for the FDM method. One may counteract this by using the discrete cosine transform (DCT), which inherently allows for Neumann boundary conditions [63]. Both methods were tested, and finally the former was used (validation provided in Appendix A). Upon taking the Fourier transform, one obtains Equation (11) (see also [64]).

$$\mathscr{F}(\mathscr{L}(D)) = \mathscr{F}(\mathcal{G}) \Rightarrow \mathscr{F}(\mathscr{L}(D)) = \widehat{\mathcal{G}(k)}, \quad \text{where } k = \frac{2\pi}{L}, \quad L \in x, y, z \tag{11}$$

Next, using properties of the Fourier transform, the scalar potential D is obtained in the spectral space as shown in Equation (12), where $\because$ is used for "since" and $\therefore$ is used for "therefore"

$$\because \mathscr{F}(\mathscr{L}(D)) = -|k|^2 \widehat{D(k)} \qquad \therefore \widehat{D(k)} = -\frac{\widehat{\mathcal{G}(k)}}{|k|^2} \tag{12}$$

The gradient ∇D can then be obtained in Fourier space by a simple multiplication by wavenumber, as shown in Equation (13). The gradient using the Fourier method was comparable to the FDM method (Figure A2).

$$\nabla \widehat{D(k)} = ik\widehat{D(k)} \tag{13}$$

Lastly, upon taking the real part of the inverse Fourier transform of Equation (13), the gradient ∇D is obtained in the spatial domain, as shown in Equation (14).

$$\nabla D = \Re(\mathscr{F}^{-1}\left(ik\widehat{D(k)}\right)) \tag{14}$$

Finally, $\bar{r}$ is found as $\bar{\zeta} - \nabla D$, and the divergence-free wind field is obtained. As discussed in Section 1, the changes to the wind field upon the divergence correction may be significant and unacceptable in certain regions. Thus, an iterative method is proposed, constraining the correction to a said bound (C) for deviation from the original wind field. The proposed method utilized in this study is shown in Algorithm 1. The algorithm uses the validated and efficient Fourier domain method[3] (see validation in Appendix A), instead of the typically used FDM method. However, the user may choose to use the FDM method if desired.

ALGORITHM 1 | Constrained divergence-free correction to wind field.

Input: Original wind field $\bar{\zeta} = (u, v, w)$
Compute divergence: $\nabla \cdot \bar{\zeta}$
Perform Helmholtz decomposition:
  Solve for D in $\nabla^2 D = \nabla \cdot \bar{\zeta}$
  Compute ∇D
  Compute new wind field: $\bar{r} = \bar{\zeta} - \nabla D$
repeat
  Compute RMSE of the wind field:
  $$\text{RMSE} = \sqrt{\frac{1}{N} \sum \| \bar{r} - \bar{\zeta} \|^2}$$
  Compute scaling factor:
  $$s = \min\left(1, \frac{C}{\| \bar{r} - \bar{\zeta} \| + \text{tol}}\right)$$
  Update $\bar{r}$:
  $$\bar{r} = \bar{\zeta} + s\left(\bar{r} - \bar{\zeta}\right)$$
  Compute divergence: $\nabla \cdot \bar{r}$
until $\| \nabla \cdot \bar{r}_{\text{new}} - \nabla \cdot \bar{r}_{\text{old}} \| \leq \text{tol}$
Output: Divergence-free wind field $\bar{r}$

2.3 | Aeroelastic Simulations

The wind turbine aeroelastic simulations were performed using NREL OpenFAST [65], a widely used open-source aero-hydro-servo-elastic tool. The v1.0.1 IEA 22-MW reference wind turbine (RWT) [47, 48], with a hub height of 170 m and a rotor diameter of 280 m, was chosen for this study. The wind turbine operation was analyzed during below-, at-, and above-rated wind speed conditions. The blade element momentum theory along with the time-dependent Øye's dynamic inflow model (see [66] for details) was used for the aerodynamic calculations. The Beddoes–Leishman dynamic stall model with the Minnema/Pierce variant (see [67] for more information) was used for incorporating the effects of dynamic stall. The module ElastoDyn, using the Euler–Bernoulli beam, was used for the structural calculations. The simulations were run for 700 s and the first 100 s were discarded as start-up transients.

3 | Wind Field Characteristics

As outlined earlier, this study considers 54 distinct wind fields. This section presents and analyzes the results for the subset corresponding to wind fields that utilize the SHIW0 coherence function illustrated in Equation (3). The divergence-free wind fields were obtained using the previously explained Algorithm 1.[3] Firstly, assessing the divergence ($\nabla \cdot \bar{\zeta}$) is relevant. The divergence magnitude is displayed in Figure 1, consistent with the above-discussed Poisson solvers; a fourth-order numerical scheme was employed. As seen in Figure 1, the proposed algorithm corrects synthetic wind fields for incompressibility. The reduction order was found to be two orders, leading to a decrease

in divergence from $\mathcal{O}(10^{-1})$ to $\mathcal{O}(10^{-3})$. The latter is also an order of magnitude observed in measurement data, for example, as seen in [68] where the authors report contours of horizontal divergence of $\mathcal{O}(10^{-3})$. These results demonstrate that the constrained algorithm successfully achieves its intended objective. In Figure 1, only a subset of the domain was shown, as indicated by the axis labels, to limit the number of points displayed. An insight into the divergence magnitude throughout the domain is shown in Figure 2. The histogram shows the narrow scatter of divergence distributed around 2 orders of magnitude lower than the original wind field. The higher divergence values were primarily observed at the domain edges and in regions of high velocity gradients inherited from the original wind field. The instantaneous wind velocity components in the center of the domain and, at hub height, that is, at 170 m are shown in Figure 3. The deviations from the original wind field are restricted by the constraint, C, in Algorithm 1. The constraint parameter C used in Algorithm 1 was set to 0.25 m/s for the u component and 0.5 m/s

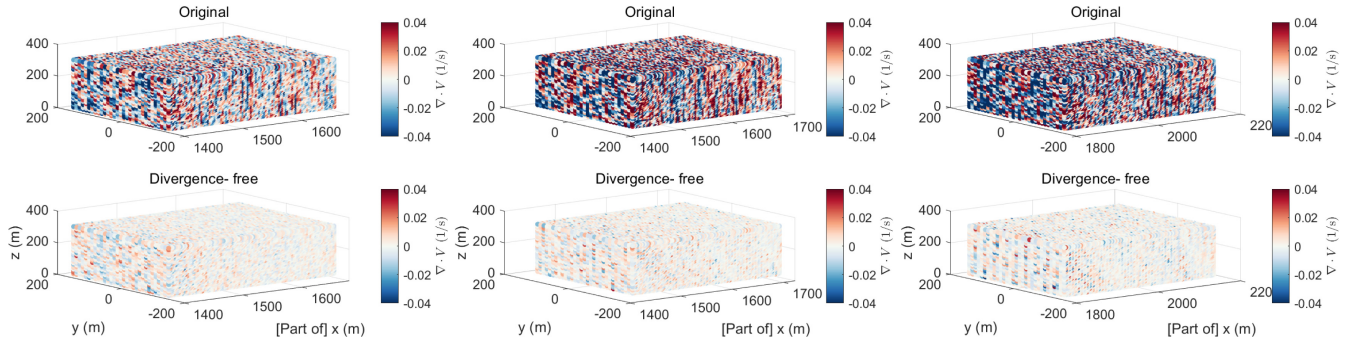

(a) Below rate doperating condition (b) At rate doperating condition (c) Above rated operating condition

FIGURE 1 | Wind field divergence throughout the domain of the SHIW0 coherence model-based wind field, in three different wind speed conditions.

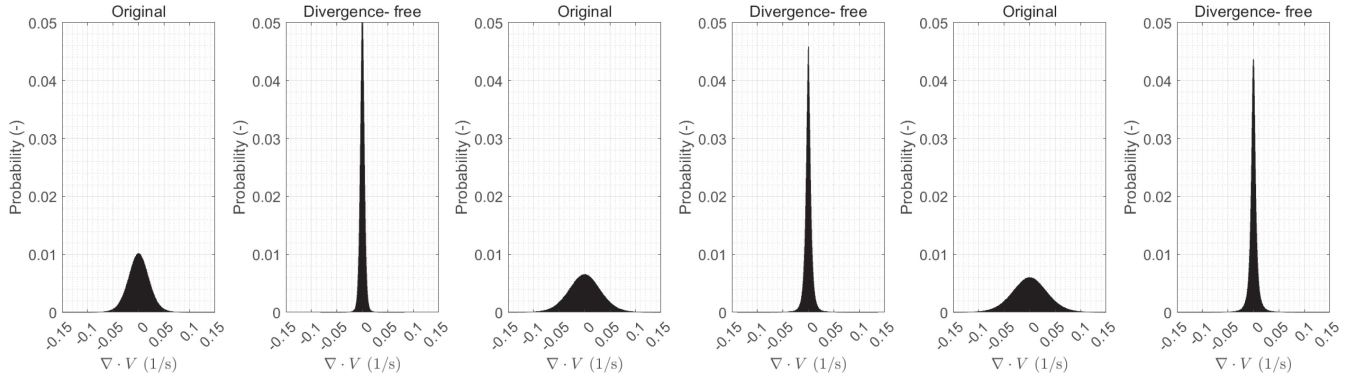

(a) Below rated operating condition (b) At rated operating condition (c) Above rated operating condition

FIGURE 2 | Histogram of the wind field divergence throughout the domain of the SHIW0 coherence model-based wind field, in three different wind speed conditions.

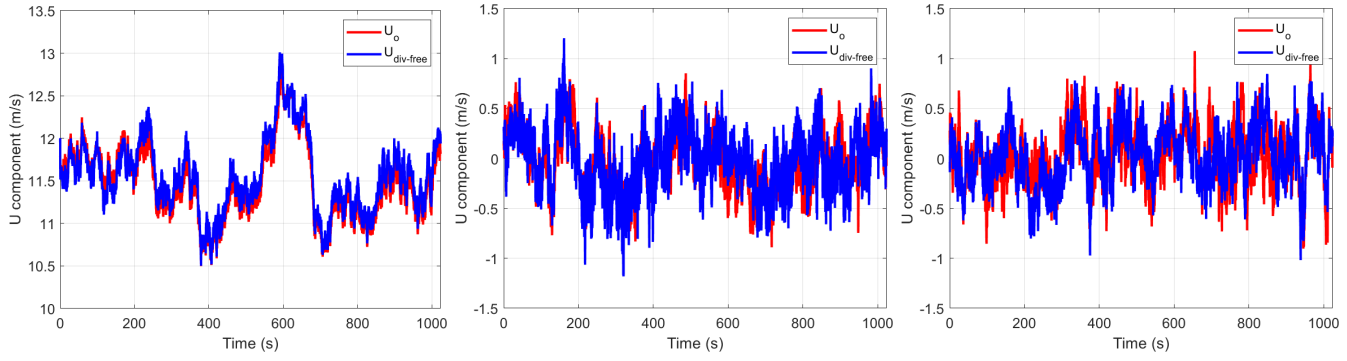

(a) u component (b) v component (c) w component

FIGURE 3 | Comparison of the instantaneous u, v, and w components of the SHIW0 coherence model-based wind field with hub-height wind speed corresponding to the at-rated operating condition.

for v and w components, higher for the latter two due to their relatively low influence on wind loads. This limit was found to limit changes to the wind field while providing the divergence reduction by 2 orders of magnitude and limiting the changes to the energy spectrum. One may vary this parameter to achieve the desired changes in the wind field. Next, two crucial first-order statistics of the wind field are shown in Figure 4. The wind shear is demonstrated by the planar average stream-wise wind component along altitude, and the standard deviation of the stream-wise wind component is shown at the span corresponding to the nacelle. It can be noted that the divergence-correction algorithm causes subtle changes in the wind field that are not directly evident from the instantaneous values or the mean values. This is particularly true for the results of the unconstrained algorithm, as discussed in Appendix B, similar to many model results reported in the literature. With the constrained algorithm, most differences in standard deviations in the wind field across the rotor span are within 10%. This is a desirable characteristic, as the wind turbine aeroelastic response is known to depend on variations in altitude, especially for large wind turbines. Another important wind field characteristic is the energy spectrum. In previous studies, it has been reported that the wind field energy spectrum magnitude reduces upon the divergence correction ([20, 69]). Although not reported, in [38], one can note the variations to the energy spectrum using the divergence-correction algorithm. In Figure 5, it can be seen that the energy spectrum of the u component of the divergence-free wind fields has an excellent match with the original wind field, but noticeable differences are observed in the high frequency region of the v component energy spectrum, and some differences are seen in the high frequency region of w component energy spectrum. These differences can, however, be reduced by controlling the C parameter in the Algorithm 1. In [49, 70, 71], the importance of low-frequency part of the u component energy spectrum was reported, thus, establishing the spectra match as one of the necessary criterion for an acceptable divergence-free correction.

The wind field spatial correlation was assessed. In Figure 6, the spanwise correlation of the wind field u component is shown at hub height. Overall, the comparison shows similar decay in the divergence-free wind field compared to the original wind field. Some regions of different zero-crossings can be identified (also observed in [20]), which lead to different integral length scales (L_u^y). These were estimated using Equation (5), and the differences in the original and divergence-free wind fields were within 5% in most instances. Next, the stream-wise correlation was assessed, and the stream-wise integral length scale (L_u^x) is shown in Figure 7. It can be observed that the integral length scales differ at higher altitudes, which correspond to higher velocities in the inflow (Figure 4). Maximum differences in L_u^x in the original and divergence-free wind fields were found to be 10%, which are thought not to alter wind turbine loads significantly and have a lesser impact on wind turbine loads than the differences in turbulence [72].

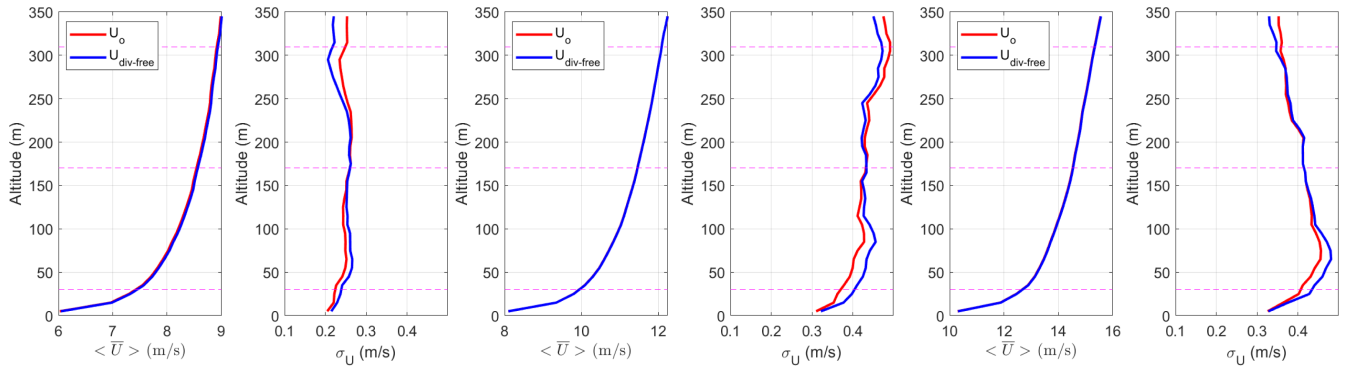

(a) Below rated operating condition (b) At rated operating condition (c) Above rated operating condition

FIGURE 4 | Comparison of mean and standard deviation of the SHIW0 coherence model-based wind field with hub-height wind speed corresponding to different operating conditions.

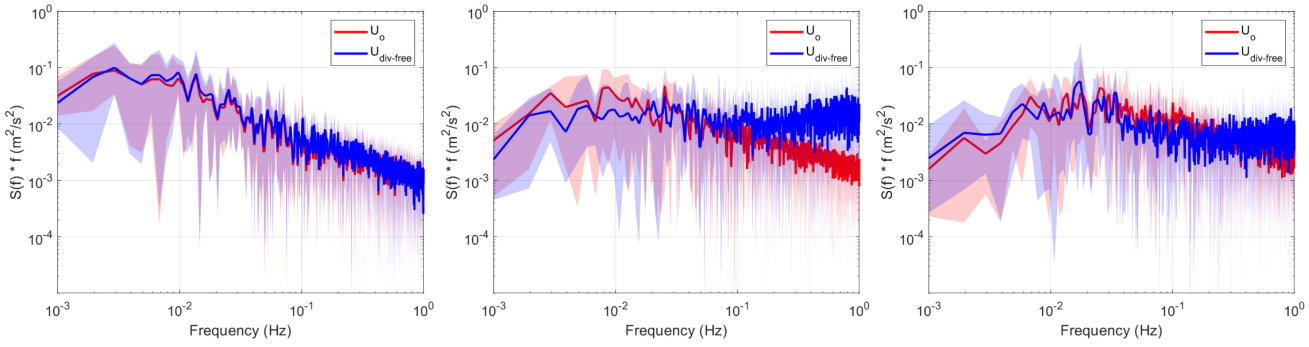

(a) u component (b) v component (c) w component

FIGURE 5 | Comparison of energy spectra of the u, v, and w components of the SHIW0 coherence model-based wind field with hub-height wind speed corresponding to the at-rated operating condition.

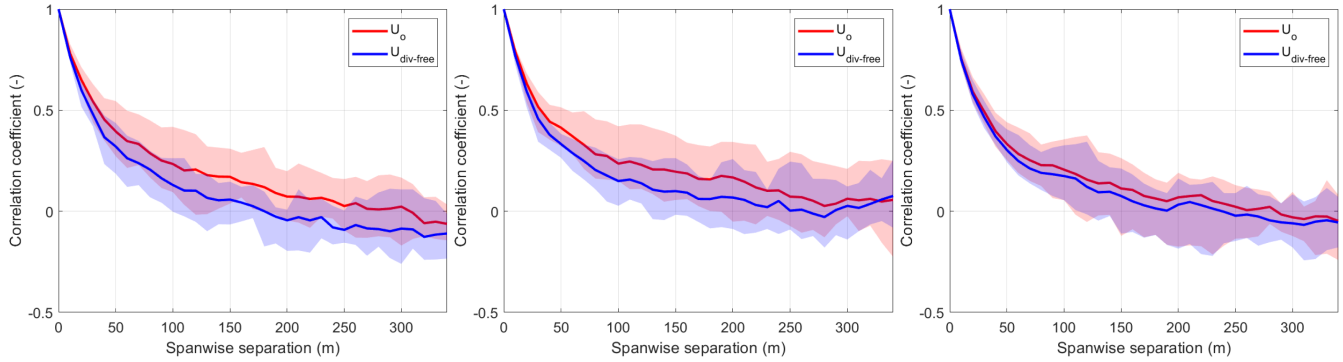

(a) Below rated operating condition (b) At rated operating condition (c) Above rated operating condition

FIGURE 6 | Comparison of spanwise correlation of the u component in the SHIW0 coherence model-based wind field with hub-height wind speed corresponding to different operating conditions.

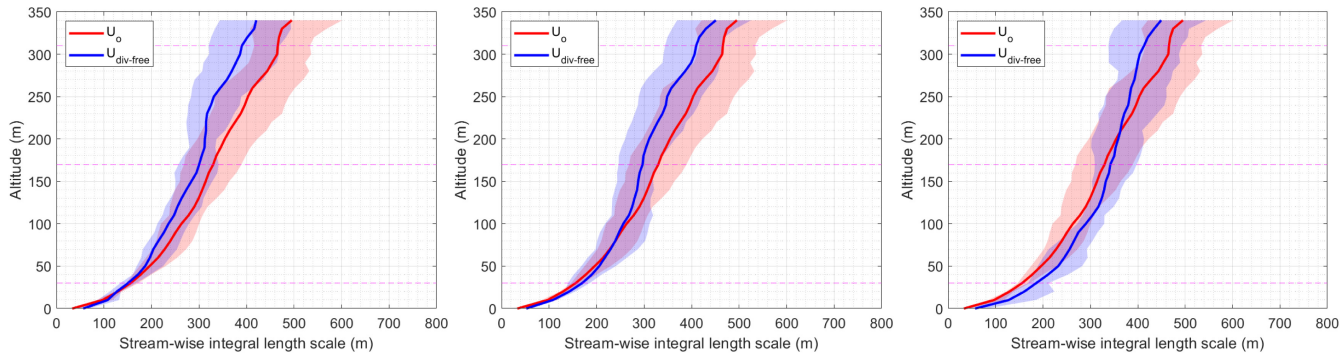

(a) Below rated operating condition (b) At rated operating condition (c) Above rated operating condition

FIGURE 7 | Comparison of stream-wise integral length scale of the u component in the SHIW0 coherence model-based wind field with hub-height wind speed corresponding to different operating conditions.

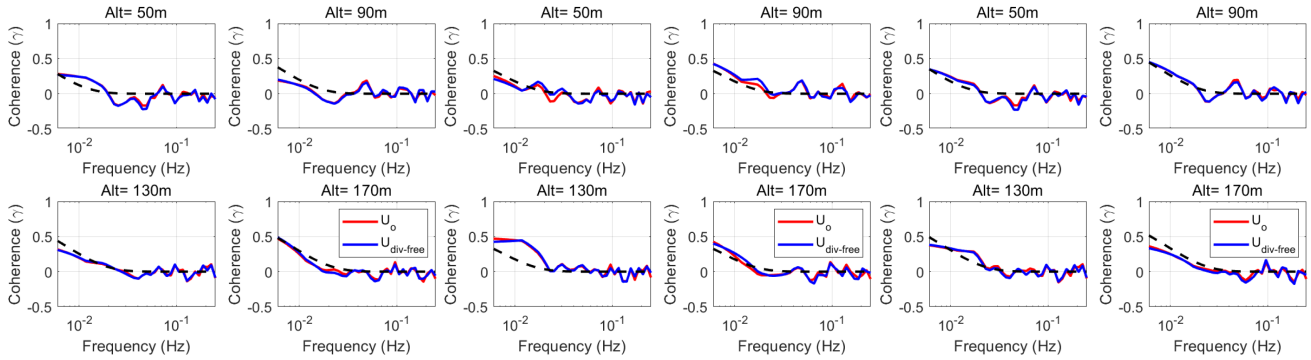

(a) SHIW0 coherence model (b) IEC Kaimal coherence model (c) SHIW1 coherence model

FIGURE 8 | Comparison of the lateral coherence (γ_{uu}) in the different coherence model-based wind fields with hub-height wind speed corresponding to the at-rated operating condition. The different subplots in each figure indicate the coherence estimates for points separated by 60 m at different altitudes. The black line indicates the theoretical coherence.

Another important second-order wind field statistic, the coherence, is compared for the original and divergence-free wind fields. In Figure 8, the lateral coherence at various altitudes is shown for a separation of 60 m. Once again, an excellent match between coherence in the original and the divergence-free wind field is evident. Some deviations from the theoretical coherence can be seen, which are thought to be due to inaccuracies in coherence estimation due to finite signal length and windowing effects. The original and divergence-free wind fields exhibit similar coherence through the different coherence functions based wind fields. This is another desired characteristic owing to the wind turbine load sensitivity to coherent structures [49, 73, 74].

Next, the lateral coherence of the v component is shown for separation of 60 m, at different altitudes, in Figure 9. Given that the constrained algorithm in this study was optimized for

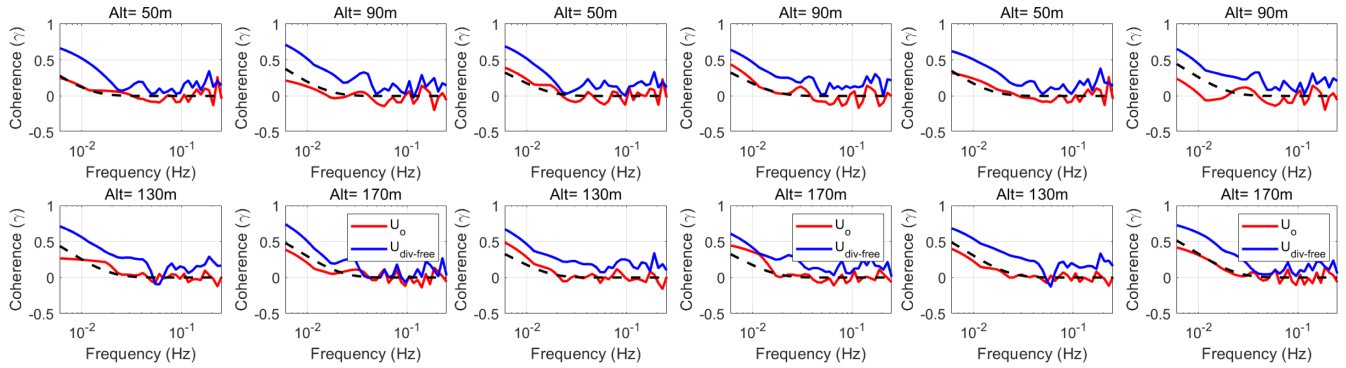

(a) SHIW0 coherence model (b) IEC Kaimal coherence model (c) SHIW coherenc e model

FIGURE 9 | Comparison of the lateral coherence (γ_{vv}) in the different coherence model-based wind fields with hub-height wind speed corresponding to the at-rated operating condition. The different subplots in each figure indicate the coherence estimates for points separated by 60 m at different altitudes. The black line indicates the theoretical coherence.

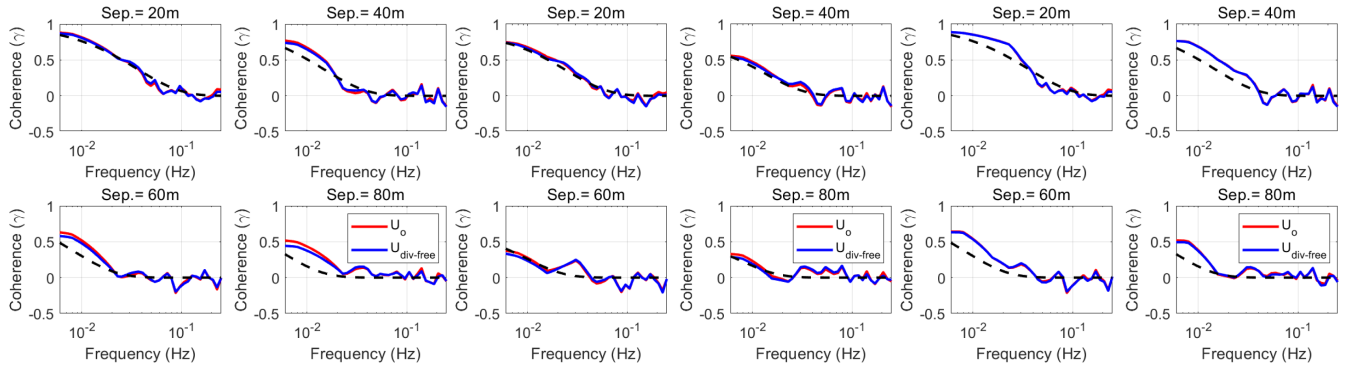

(a) SHIW0 coherence model (b) IEC Kaimal coherence model (c) SHIW1 coherence model

FIGURE 10 | Comparison of the vertical coherence (γ_{uu}) in the different coherence model-based wind fields with hub-height wind speed corresponding to the at-rated operating condition. The different subplots in each figure indicate the coherence estimates for points separated by different separations, at the hub height. The black line indicates the theoretical coherence.

prioritizing matches in the stream-wise u component, differences are observed for the crosswind component. Furthermore, in Figure 9, it is observed that the v component coherence is almost always higher in the divergence-free wind field than in the original wind field. This is accompanied by a slightly higher correlation in the spanwise direction for the crosswind component (not shown here for brevity). It can be noted that the significance of the v component coherence is limited for wind turbine loads but more for wind turbine wake meandering, for instance [75–77]. Further to the point, the current IEC Kaimal coherence function does not specify use for the crosswind or the vertical wind component, but only for the stream-wise component. However, it is reported here to allow for more insights into the corrected wind fields. The next section discusses the corresponding impact on the wind turbine load channel sensitivity to this change.

The last wind field characteristic presented is the vertical coherence in wind fields. The vertical coherence at different separations is shown in Figure 10. The vertical coherence at various separations is almost the same in both the original and divergence-free wind fields. It may also be recalled that the IEC Kaimal coherence function (Equation (1)) does not distinguish between lateral and vertical coherence, nor does it account for changes in coherence with altitude, unlike the SHIW coherence function (Equation (3)).

4 | Wind Turbine Aeroelastic Response

The IEA 22 MW wind turbine aeroelastic response in the original and divergence-free wind fields is discussed here. The wind turbine loads analyzed were the blade root flap-wise bending moment (M_{flap}), the wind turbine tower base fore-aft bending moment ($M_{T_{f-a}}$), and the wind turbine tower top side-side moment (M_{T-y}).

Given the almost perfect match in the mean wind profiles (left subplots in Figure 4), the mean wind turbine loads were found to be within $\pm$ 2% from the original wind field. Thus, these are not shown in this article for brevity. The standard deviation of loads is first discussed, shown in Figure 11. In Figure 11, the dashed lines indicate the differences in loads upon use of the typical unconstrained divergence-correction algorithm. The solid lines in Figure 11 indicate the differences in loads upon use of the proposed Algorithm 1. The changes in wind field characteristics, mainly energy spectrum and the standard deviation profile, significantly change the unsteady aeroelastic response. The differences in $\sigma_{M_{T_{f-a}}}$ are found to be as large as $-$ 20% while relatively better for $\sigma_{M_{flap}}$, at $-$ 5%, for the divergence-free wind field made using the typical unconstrained algorithm. The higher impact on the $\sigma_{M_{T_{f-a}}}$ is thought to be due to the rotor sweeping through different unsteadiness in the wind profile impacting

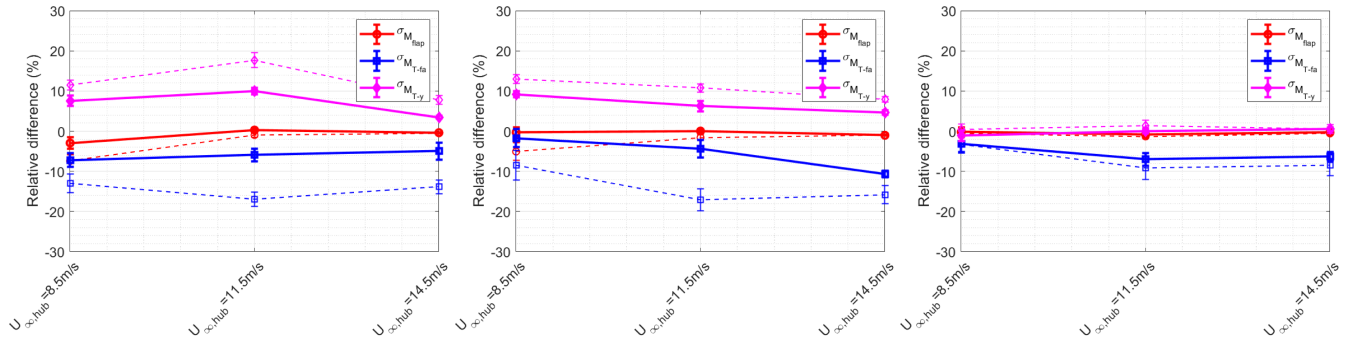

(a) SHIW0 coherence model (b) SHIW1 coherence model (c) IEC Kaimal coherence model

FIGURE 11 | Comparison of standard deviation of root flap-wise bending moment ($\sigma_{M_{flap}}$), tower fore-aft moment ($\sigma_{M_{T_{f-a}}}$) and the tower top side-side moment ($\sigma_{M_{T-y}}$). Relative differences are shown in comparison to the original wind field. Solid lines indicate the difference in load metric for the constrained algorithm-based divergence-free wind field, while dashed lines indicate the unconstrained algorithm-based divergence-free wind field.

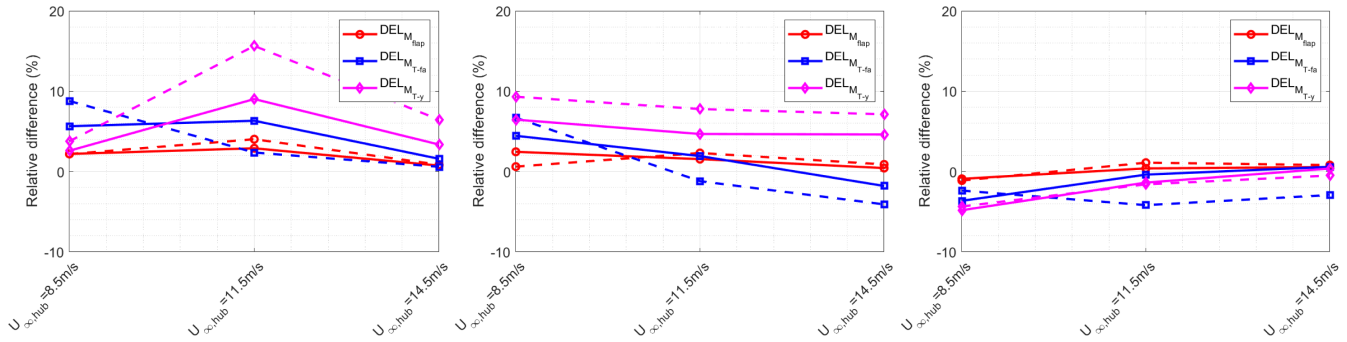

(a) SHIW0 coherence model (b) SHIW1 coherence model (c) IEC Kaimal coherence model

FIGURE 12 | Comparison of damage equivalent root flap-wise bending moment ($DEL_{M_{flap}}$), tower fore-aft moment ($DEL_{M_{T_{f-a}}}$), and the tower top side-side moment ($DEL_{M_{T-y}}$). Relative differences are shown in comparison to the original wind field. Solid lines indicate the difference in load metric for the constrained algorithm-based divergence-free wind field, while dashed lines indicate the unconstrained algorithm-based divergence-free wind field.

the overall unsteadiness in thrust and the resulting $\sigma_{M_{T_{f-a}}}$ [78]. The different unsteadiness is seen to be lower turbulence in the upper half of the rotor (right subplots in Figure 4), leading to overall higher velocities, and opposite for the bottom half of the rotor. These unsteadiness differences were observed to manifest in the azimuthal dispersion in load quantities (see Appendix D). The different unsteadiness leads to a disproportionate impact on $M_{T_{f-a}}$ given the higher moment arm for the upper half of the rotor with the higher velocities. While for the $\sigma_{M_{flap}}$, an averaging effect occurs in the two halves of the rotor. The differences in $\sigma_{M_{T-y}}$ are seen to be a noticeably higher increase (up to 20%), for the divergence-free wind field made using the typical unconstrained algorithm. However, it can also be observed that this increase is only evident for the SHIW0 and SHIW1 coherence model-based wind fields, while the differences in $\sigma_{M_{T-y}}$ are unremarkable for the IEC Kaimal coherence model-based wind field. It is hypothesized that this behavior is due to the latter model not distinguishing between coherence at different altitudes and between lateral and vertical coherence. Nevertheless, it can be seen that the improvement in wind field characteristics' comparison in the divergence-free wind field generated from Algorithm 1 leads to a noticeable decrease in discrepancy in the wind turbine aeroelastic response. Differences are still seen, at up to − 10% for the $\sigma_{M_{T_{f-a}}}$ and $\sigma_{M_{T-y}}$, and − 5% for $\sigma_{M_{flap}}$, in few instances.

Finally, to assess the fatigue loads, a fatigue assessment based on the damage equivalent load formulation (corrected for mean stress) of [79] was used with the input of M_{flap}, $M_{T_{f-a}}$, and M_{T-y}. The damage equivalent load (S_{eq}) was found using Equation (15).

$$S_{r,eq} = \left(\frac{\sum_{i=1}^{n} \left(S_{r,i} \frac{S_u - |S_{m,eq}|}{S_u - |S_{m,i}|} \right)^m}{N_{eq}} \right)^{\frac{1}{m}} \tag{15}$$

$S_{r,i}$ is the range (difference of maximum and minimum value) of the i^{th} load cycle, and $S_{m,i}$ is the mean of the i^{th} load cycle. N_{eq} was chosen as 10^7 [80] and $S_{m,eq}$ as 0. Finally, to select S_u, the authors propose to evaluate it at different $\frac{S_{max}}{S_u}$ ratios. So, the value of S_{max} is used, corresponding to the maximum moment in the respective case, different for each wind speed bin. The value of S_{max}, which corresponds to the maximum bending moment for the respective wind speed was chosen and $\frac{S_u}{S_{max}} = 0.4$ along with a Wöhler exponent of $m = 10$ for the flap-wise bending moment and $m = 4$ for the tower base fore-aft bending moment and the tower top side-side moment [81]. Following the discussion on the standard deviation of loads shown in Figure 11, a similar trend is seen in the damage equivalent loads (shown in Figure 12), but with a lower change. Once again, lower differences are seen

for M_{flap} up to 3% and slightly higher up to 6% for $M_{T_{f-a}}$ and 10% for M_{T-y}, when using the constrained divergence-correction algorithm. This discussion suggests that the proposed algorithm largely preserves the wind field characteristics after the incompressibility correction. Potential improvements remain and are considered in future work listed in Section 5.

5 | Conclusions and Recommendations

This article addresses the issue of divergence in synthetic wind fields, that is, incompatibility with the incompressibility condition. A literature overview highlights the importance of ensuring divergence-free wind fields to improve the reliability of their use in CFD and wind load simulations and enhance the overall realism of synthetic wind fields. The standard approach involves a posteriori correction applied to the generated wind field.

In this study, synthetic wind fields were generated using Shinozuka and Deodatis's spectral method. The wind fields were temporally and spatially correlated, employing energy spectra and coherence functions. Helmholtz–Hodge decomposition was conducted to find the incompressible wind field. A Poisson equation solver was implemented using the typical FDM and Fourier methods. The motivation for the latter implementation was computational efficiency, especially considering that the Poisson equation needs to be solved iteratively to reach convergence. The solver was validated on a manufactured example and a case of divergence correction to the synthetic wind field.

The divergence-correction procedure introduces subtle but significant differences in the wind field, which can lead to substantial differences in wind loads on the object. As reported in the literature, this correction often causes a drop in the energy spectrum, alters the unsteady wind profile with height, and affects other second-order characteristics. Although various studies have attempted to address these issues, they remain an area of ongoing research. This article proposes a constrained divergence-correction algorithm, introducing an iterative process that limits deviations from the original wind field within user-defined bounds. While discrepancies are significantly reduced compared to conventional methods, some differences persist, though within a more acceptable range.

The algorithm was comprehensively used on a total of 54 different wind fields, differing in wind speeds, coherence functions, and random seeds. The algorithm could achieve a three-order reduction in divergence and maintain several first- and second-order wind field statistics. The changes to the standard deviation of the wind profile were reduced from up to − 20% to − 8%. The resulting wind fields were input to aeroelastic simulations for further investigation into the impact of wind field changes on the IEA 22 MW wind turbine. The changes to mean wind loads were unremarkable, but this was not the case for the standard deviation of loads. The wind loads with use of the divergence-free wind fields generated from the proposed constrained algorithm showed deviations from the wind loads with the original wind field, at up to − 10% for the standard deviation of the tower base fore-aft bending moment ($\sigma_{M_{T_{f-a}}}$), maximal 10% for the standard deviation of the tower top side-side bending moment ($\sigma_{M_{T-y}}$) and maximal − 5% for the standard deviation of root flap-wise bending moment ($\sigma_{M_{flap}}$). The wind loads with use of the divergence-free wind fields generated from the typically used unconstrained algorithm showed significant differences up to − 20% for $\sigma_{M_{T_{f-a}}}$, up to + 20% for $\sigma_{M_{T-y}}$ and − 5% for $\sigma_{M_{flap}}$.

Regarding the validated solver, an efficient algorithm and implementation for a posteriori divergence correction on synthetic wind fields is proposed in this study. Future work will focus on integrating this algorithm into the step of wind field generation rather than being a posteriori step. Furthermore, a parallel algorithm implementation of the solver will be beneficial for further speedup. Future work will also attempt to incorporate control over specific wind field characteristics at user discretion.

Disclosure

This research was supported by the Korea Institute of Energy Technology Evaluation and Planning (KETEP) grant funded by the Korea Government (MOTIE) (20228520020050). The authors thank the Delft High-Performance Computing Centre [82] for the use of computational resources of the DelftBlue supercomputer. The authors thank SURF (www.surf.nl) for the support in using the Dutch National Supercomputer Snellius.

Conflicts of Interest

The authors declare no conflicts of interest.

Data Availability Statement

The data that support the findings of this study are available from the corresponding author upon request.

Peer Review

The peer review history for this article is available at https://www.webofscience.com/api/gateway/wos/peer-review/10.1002/we.70062.

Endnotes

[1] A formal merger of the Helmholtz decomposition of vector fields [28, 29] and the Hodge decomposition (named after W. V. D. Hodge, and similar to Helmholtz decomposition but for differential forms) do not appear to have a clear origin, as also stated by [30]. This approach may be linked to [31] as suggested by [32]

[2] A further detailed implementation of this approach for the divergence-free correction is described in Subsection 2.2

[3] This allowed for up to 5 times speed-up and less memory overhead, enabling the algorithm to run for the 5 million element domain within 10 min on a personal computer. Please note that the algorithm is not yet coded in a manner suitable for parallel processing. Thus, the computational expense reported is for serial processing.

[4] An example of results using the typical, non-constrained algorithm is shown in Figure 1, highlighting the need for the constrained algorithm.

References

1. G. R. Tabor and M. H. Baba-Ahmadi, "Inlet Conditions for Large Eddy Simulation: A Review," *Computers and Fluids* 39, no. 4 (2010): 553–567, https://doi.org/10.1016/J.COMPFLUID.2009.10.007.

2. L. Patruno and M. Ricci, "A Systematic Approach to the Generation of Synthetic Turbulence Using Spectral Methods," *Computer Methods in Applied Mechanics and Engineering* 340 (2018): 881–904, https://doi.org/10.1016/J.CMA.2018.06.028.

3. X. Wu, "Inflow Turbulence Generation Methods," *Annual Review of Fluid Mechanics* 49 (2017): 23–49, https://doi.org/10.1146/annurev-fluid-010816-060322, https://cfd.spbstu.ru/agarbaruk/doc/2017_Wu_Inflow%20Turbulence%20Generation%20Methods.pdf.

4. N. S. Dhamankar, G. A. Blaisdell, and A. S. Lyrintzis, "Overview of Turbulent Inflow Boundary Conditions for Large-Eddy Simulations," *AIAA Journal* 56, no. 4 (2018): 1317–1334, https://doi.org/10.2514/1.J055528/ASSET/IMAGES/LARGE/FIGURE4.JPEG.

5. A. Montorfano, F. Piscaglia, and G. Ferrari, "Inlet Boundary Conditions for Incompressible LES: A Comparative Study," *Mathematical and Computer Modelling* 57, no. 7–8 (2013): 1640–1647, https://doi.org/10.1016/J.MCM.2011.10.077.

6. R. Vasaturo, I. Kalkman, B. Blocken, and P. J. V. van Wesemael, "Large Eddy Simulation of the Neutral Atmospheric Boundary Layer: Performance Evaluation of Three Inflow Methods for Terrains With Different Roughness," *Journal of Wind Engineering and Industrial Aerodynamics* 173 (2018): 241–261, https://doi.org/10.1016/J.JWEIA.2017.11.025.

7. F. McKenna, K. Zhong, M. Gardner, et al., "NHERI-SimCenter/WE-UQ: Version 4.1.0". doi: https://doi.org/10.5281/ZENODO.13865388.

8. G. G. Deierlein, F. McKenna, A. Zsarnóczay, et al., "A Cloud-Enabled Application Framework for Simulating Regional-Scale Impacts of Natural Hazards on the Built Environment," *Frontiers in Built Environment* 6 (2020): 558706, https://doi.org/10.3389/FBUIL.2020.558706.

9. M. Hoshiya, "Simulation of Multi-Correlated Random Processes and Application to Structural Vibration Problems*". In: Proc. of JSCE 204 (1972).

10. M. Shinozuka and C.-M. Jan, "Digital Simulation of Random Processes and Its Applications," *Journal of Sound and Vibration* 25, no. 1 (1972): 111–128, https://doi.org/10.1016/0022-460X(72)90600-1, https://ui.adsabs.harvard.edu/abs/1972JSV....25..111S/abstract.

11. T. S. Lund, X. Wu, and K. D. Squires, "Generation of Turbulent Inflow Data for Spatially-Developing Boundary Layer Simulations," *Journal of Computational Physics* 140, no. 2 (1998): 233–258, https://doi.org/10.1006/JCPH.1998.5882.

12. M. Klein, A. Sadiki, and J. Janicka, "A Digital Filter Based Generation of Inflow Data for Spatially Developing Direct Numerical or Large Eddy Simulations," *Journal of Computational Physics* 186, no. 2 (2003): 652–665, https://doi.org/10.1016/S0021-9991(03)00090-1.

13. N. Jarrin, S. Benhamadouche, D. Laurence, and R. Prosser, "A Synthetic-Eddy-Method for Generating Inflow Conditions for Large-Eddy Simulations," *International Journal of Heat and Fluid Flow* 27, no. 4 (2006): 585–593, https://doi.org/10.1016/J.IJHEATFLUIDFLOW.2006.02.006, https://research.manchester.ac.uk/en/publications/a-synthetic-eddy-method-for-generating-inflow-conditions-for-larg.

14. R. H. Kraichnan, "Diffusion by a Random Velocity Field," *Physics of Fluids* 13, no. 1 (1970): 22–31, https://doi.org/10.1063/1.1692799.

15. A. K. Dagnew and G. T. Bitsuamlak, "Computational Evaluation of Wind Loads on a Standard Tall Building Using LES," *Wind and Structures* 18, no. 5 (2014): 567–598, https://doi.org/10.12989/WAS.2014.18.5.567.

16. A. Smirnov, S. Shi, and I. Celik, "Random Flow Generation Technique for Large Eddy Simulations and Particle-Dynamics Modeling," *Journal of Fluids Engineering* 123, no. 2 (2001): 359–371, https://doi.org/10.1115/1.1369598.

17. R. Poletto, T. Craft, and A. Revell, "A New Divergence Free Synthetic Eddy Method for the Reproduction of Inlet Flow Conditions for LES," *Flow, Turbulence and Combustion* 91, no. 3 (2013): 519–539, https://doi.org/10.1007/S10494-013-9488-2.

18. J. Friedrich, D. Moreno, M. Sinhuber, M. Wächter, and J. Peinke, "Superstatistical Wind Fields From Pointwise Atmospheric Turbulence Measurements," *PRX Energy* 1, no. 2 (2022): 023006, https://doi.org/10.1103/PRXENERGY.1.023006.

19. Benoit 'Commandant, "Note Sur Une Méthode de Résolution des équations Normales Provenant de L'Application de la MéThode des Moindres Carrés a un Système D'équations Linéaires en Nombre Inférieur a Celui des Inconnues. - Application de la Méthode a la Résolution D'un Système Defini D'éQuations LinéAires (procédé du commandant Cholesky)," *Bulletin géodésique* 2, no. 1 (1924): 67–77, https://doi.org/10.1007/BF03031308/METRICS.

20. K. Kondo, S. Murakami, and A. Mochida, "Generation of Velocity Fluctuations for Inflow Boundary Condition of LES," *Journal of Wind Engineering and Industrial Aerodynamics* 67-68 (1997): 51–64, https://doi.org/10.1016/S0167-6105(97)00062-7.

21. L. Patruno and M. Ricci, "On the Generation of Synthetic Divergence-Free Homogeneous Anisotropic Turbulence," *Computer Methods in Applied Mechanics and Engineering* 315 (2017): 396–417, https://doi.org/10.1016/J.CMA.2016.11.005.

22. P. M. Gresho and R. L. Sani, "On Pressure Boundary Conditions for the Incompressible Navier-Stokes Equations," *International Journal for Numerical Methods in Fluids* 7, no. 10 (1987): 1111–1145, https://doi.org/10.1002/FLD.1650071008.

23. E. Shirani, J. H. Ferziger, and W. C. Reynolds, "Mixing of a Passive Scalar in Isotropic and Sheared Homogeneous Turbulence". Tech. rep. 1981. url: https://ntrs.nasa.gov/citations/19820003521.

24. Y. Kim, I. P. Castro, and Z. T. Xie, "Divergence-Free Turbulence Inflow Conditions for Large-Eddy Simulations With Incompressible Flow Solvers," *Computers and Fluids* 84 (2013): 56–68, https://doi.org/10.1016/J.COMPFLUID.2013.06.001.

25. X. Zheng Tong and I. P. Castro, "Efficient Generation of Inflow Conditions for Large Eddy Simulation of Street-Scale Flows," *Flow, Turbulence and Combustion* 81, no. 3 (2008): 449–470, https://doi.org/10.1007/S10494-008-9151-5/METRICS.

26. R. I. Issa, "Solution of the Implicitly Discretised Fluid Flow Equations by Operator-Splitting," *Journal of Computational Physics* 62, no. 1 (1986): 40–65, https://doi.org/10.1016/0021-9991(86)90099-9.

27. C. Rosales and C. Meneveau, "A Minimal Multiscale Lagrangian Map Approach to Synthesize Non-Gaussian Turbulent Vector Fields," *Physics of Fluids* 18, no. 7 (2006): 075104-1–075104-16, https://doi.org/10.1063/1.2227003/256337.

28. H. Helmholtz, "Über Integrale der hydrodynamischen Gleichungen, welche den Wirbelbewegungen entsprechen," *Journal Für Die Reine Und Angewandte Mathematik* 55 (1858): 25–55, https://eudml.org/doc/147720.

29. H. Helmholtz, "LXIII. On Integrals of the Hydrodynamical Equations, Which Express Vortex-Motion," *London, Edinburgh, and Dublin Philosophical Magazine and Journal of Science* 33, no. 226 (1867): 485–512, https://doi.org/10.1080/14786446708639824.

30. H. Bhatia, G. Norgard, V. Pascucci, and P.-T. Bremer, "The Helmholtz-Hodge Decomposition—A Survey," *IEEE Transactions on Visualization and Computer Graphics* 19 (2012): 1386–1404, https://doi.org/10.1109/TVCG.2012.316, https://www.sci.utah.edu/~hbhatia/pubs/2013_TVCG_survey.pdf.

31. O. A. Ladyzhenskaja, *The Mathematical Theory of Viscous Incompressible Flow*, ed. 2nd ed. (Gordon and Breach, 1963), https://archive.org/details/mathematicaltheo0000lady/page/n5/mode/2up.

32. F. M. Denaro, "On the Application of the Helmholtz–Hodge Decomposition in Projection Methods for Incompressible Flows With General Boundary Conditions," *International Journal for Numerical Methods in Fluids* 43, no. 1 (2003): 43–69, https://doi.org/10.1002/FLD.598.

33. E. Branlard, E. Quon, A. R. Meyer Forsting, J. King, and P. Moriarty, "Wind Farm Blockage Effects: Comparison of Different Engineering Models," *Journal of Physics: Conference Series* 1618, no. 6 (2020): 062036, https://doi.org/10.1088/1742-6596/1618/6/062036.

34. Chorin, Alexandre J. and Marsden, Jerrold E. A Mathematical Introduction to Fluid Mechanics. In: Texts in Applied Mathematics 4 (1993), https://doi.org/10.1007/978-1-4612-0883-9.

35. P. J. Roache, "A Pseudo-Spectral FFT Technique for Non-Periodic Problems," *Journal of Computational Physics* 27, no. 2 (1978): 204–220, https://doi.org/10.1016/0021-9991(78)90005-0.

36. H. Fu and C. Liu, "A Buffered Fourier Spectral Method for Non-Periodic PDE," *International Journal of Numerical Analysis and Modeling* 9, no. 2 (2012): 460–478, https://doi.org/10.2514/6.2012-576.

37. D. S. Balsara and J. Kim, "A Comparison Between Divergence-Cleaning and Staggered-Mesh Formulations for Numerical Magnetohydrodynamics," *Astrophysical Journal* 602, no. 2 (2004): 1079–1090, https://doi.org/10.1086/381051/FULLTEXT/.

38. F. M. Abiy and T. B. Girma, "A Divergence-Free Inflow Turbulence Generator Using Spectral Representation Method for Large-Eddy Simulation of ABL Flows," *Journal of Wind Engineering and Industrial Aerodynamics* 212 (2021): 104580, https://doi.org/10.1016/J.JWEIA.2021.104580.

39. G. Lamberti, C. García-Sánchez, J. Sousa, and C. Gorlé, "Optimizing Turbulent Inflow Conditions for Large-Eddy Simulations of the Atmospheric Boundary Layer," *Journal of Wind Engineering and Industrial Aerodynamics* 177 (2018): 32–44, https://doi.org/10.1016/J.JWEIA.2018.04.004.

40. International Electrotechnical Commission (IEC). "IEC 61400–3-1:2019|IEC Webstore". url: https://webstore.iec.ch/publication/29360.

41. J. Mann, "The Spatial Structure of Neutral Atmospheric Surface-Layer Turbulence," *Journal of Fluid Mechanics* 273 (1994): 141–168, https://orbit.dtu.dk/en/publications/the-spatial-structure-of-neutral-atmospheric-surface-layer-turbul.

42. J. Mann, "Wind Field Simulation," *Probabilistic Engineering Mechanics* 13, no. 4 (1998): 269–282, https://doi.org/10.1016/S0266-8920(97)00036-2.

43. J. C. Kaimal, J. C. Wyngaard, Y. Izumi, and O. R. Coté, "Spectral Characteristics of Surface-Layer Turbulence," *Quarterly Journal of the Royal Meteorological Society* 98, no. 417 (1972): 563–589, https://doi.org/10.1002/QJ.49709841707.

44. R. Thresher, W.E. Holley, C.E. Smith, N. Jafarey, S.R. Lin "Modeling the Response of Wind Turbines to Atmospheric Turbulence". In: (May 1981).

45. A. G. Davenport, "The Application of Statistical Concepts to the Wind Loading of Structures," *Proceedings of the Institution of Civil Engineers* 19, no. 4 (1961): 449–472, https://doi.org/10.1680/iicep.1961.11304.

46. G. Lasse, "TuGen: Synthetic Turbulence Generator, Manual and User's Guide". Tech. Rep. Aalborg: Department of Civil Engineering, Aalborg University, (2009), https://vbn.aau.dk/en/publications/tugen-synthetic-turbulence-generator-manual-and-users-guide.

47. IEA Wind Task 37, "IEAWindTask37/IEA-22-280-RWT" (2023) url: https://github.com/IEAWindTask37/IEA-22-280-RWT.

48. F. Zahle, T. Barlas, K. Lonbaek, et al., "Definition of the IEA Wind 22-Megawatt Offshore Reference Wind Turbine". In: (2024). https://doi.org/10.11581/DTU.00000317.

49. N. Dangi, J. Sodja, C. S. Ferreira, and W. Yu, "The Effect of Turbulent Coherent Structures in Atmospheric Flow on Wind Turbine Loads," *Renewable Energy* 241 (2025): 122248, https://doi.org/10.1016/j.renene.2024.122248.

50. Panofsky, Hans A and Dutton, John A. *Atmospheric Turbulence: Models and Methods for Engineering Applications* (John Wiley & Sons, 1984).

51. International Electrotechnical Commission (IEC) "IEC 61400-1:2019" (2019) url: https://webstore.iec.ch/publication/26423.

52. K. Saranyasoontorn, L. Manuel, and P. S. Veers, "A Comparison of Standard Coherence Models for Inflow Turbulence With Estimates From Field Measurements," *Journal of Solar Energy Engineering* 126, no. 4 (2004): 1069–1082, https://doi.org/10.1115/1.1797978.

53. E. Cheynet "WindSimFaster: WindSimFast, but Faster—File Exchange—MATLAB Central" 2024 https://nl.mathworks.com/matlabcentral/fileexchange/163676-windsimfaster-windsimfast-but-faster.

54. J. Wang, E. Cheynet, J. Þ. Snæbjörnsson, and J. B. Jakobsen, "Coupled Aerodynamic and Hydrodynamic Response of a Long Span Bridge Suspended From Floating Towers," *Journal of Wind Engineering and Industrial Aerodynamics* 177 (2018): 19–31, https://doi.org/10.1016/j.jweia.2018.03.024.

55. M. Shinozuka and G. Deodatis, "Simulation of Stochastic Processes by Spectral Representation," *Applied Mechanics Reviews* 44, no. 4 (1991): 191–204, https://doi.org/10.1115/1.3119501.

56. G. I. Taylor, "The Spectrum of Turbulence," *Proceedings of the Royal Society of London. Series A—Mathematical and Physical Sciences* 164, no. 919 (1938): 476–490, https://doi.org/10.1098/RSPA.1938.0032.

57. L. Kristensen and N. O. Jensen, "Lateral Coherence in Isotropic Turbulence and in the Natural Wind," *Boundary-Layer Meteorology* 17, no. 3 (1979): 353–373, https://doi.org/10.1007/BF00117924/METRICS.

58. P. D. Welch, "The Use of Fast Fourier Transform for the Estimation of Power Spectra: A Method Based on Time Averaging Over Short, Modified Periodograms," *IEEE Transactions on Audio and Electroacoustics* 15, no. 2 (1967): 70–73, https://doi.org/10.1109/TAU.1967.1161901.

59. E. Cheynet, "Wind-Induced Vibrations of a Suspension Bridge: A Case Study in Full-Scale". In: PhD thesis University of Stavanger (2016). issn: 1890–1387, https://uis.brage.unit.no/uis-xmlui/handle/11250/2425472.

60. D. H. Lenschow and B. B. Stankov, "Length Scales in the Convective Boundary Layer," *Journal of Atmospheric Sciences* 43, no. 12 (1986): 1198–1209, https://doi.org/10.1175/1520-0469(1986)043<1198:LSITCB>2.0.CO;2.

61. J. D. Hoffman, J. D. Hoffman, and S. Frankel, *Numerical Methods for Engineers and Scientists* (CRC Press, 2018), https://doi.org/10.1201/9781315274508.

62. W. S. G., G. H. Golub, and C. F. Van Loan, "Matrix Computations," *Mathematics of Computation* 56, no. 193 (1991): 224–227.

63. V. Fuka, "PoisFFT—A Free Parallel Fast Poisson Solver," *Applied Mathematics and Computation* 267 (2015): 356–364, https://doi.org/10.1016/J.AMC.2015.03.011.

64. Stein, Elias M. and Shakarchi, Rami. *Fourier Analysis: An Introduction* (Princeton University Press, 2011).

65. J. Jonkman, M. Sprague, and et al. "OpenFAST|Wind Research|NREL". 2022. url: https://www.nrel.gov/wind/nwtc/openfast.html.

66. E. Branlard, B. Jonkman, G. R. Pirrung, K. Dixon, and J. Jonkman, "Dynamic Inflow and Unsteady Aerodynamics Models for Modal and Stability Analyses in OpenFAST," *Journal of Physics: Conference Series* 2265 (2022): 032044, https://doi.org/10.1088/1742-6596/2265/3/032044, https://www.nrel.gov/docs/fy22osti/82343.pdf.

67. R. Damiani and G. Hayman, "The Unsteady Aerodynamics Module for FAST 8". In: NREL Technical Report (2019), https://www.nrel.gov/docs/fy20osti/66347.pdf.

68. L. Alcayaga, G. C. Larsen, M. Kelly, and J. Mann, "Large-Scale Coherent Turbulence Structures in the Atmospheric Boundary Layer Over Flat Terrain," *Journal of the Atmospheric Sciences* 79, no. 12 (2022): 3219–3243, https://doi.org/10.1175/JAS-D-21-0083.1.

69. E. S. P. Branlard, "Analysis of Wind Turbine Aerodynamics and Aeroelasticity Using Vortex-Based Methods". PhD thesis. Denmark: DTU Wind Energy, 2015. isbn: 9788793278448, https://orbit.dtu.dk/en/publications/analysis-of-wind-turbine-aerodynamicsand-aeroelasticity-using-vo.

70. A. Nybø, F. G. Nielsen, and M. Godvik, "Analysis of Turbulence Models Fitted to Site, and Their Impact on the Response of a Bottom-Fixed Wind Turbine," *Journal of Physics: Conference Series* 2018, no. 1 (2021): 12028, https://doi.org/10.1088/1742-6596/2018/1/012028.

71. M. C. Holtslag, W. A. A. M. Bierbooms, and G. J. W. van Bussel, "Wind Turbine Fatigue Loads as a Function of Atmospheric Conditions Offshore," *Wind Energy* 19, no. 10 (2016): 1917–1932, https://doi.org/10.1002/WE.1959.

72. B. J. Stanislawski, R. Thedin, A. Sharma, E. Branlard, G. Vijayakumar, and M. A. Sprague, "Effect of the Integral Length Scales of Turbulent Inflows on Wind Turbine Loads," *Renewable Energy* 217 (2023): 119218, https://doi.org/10.1016/J.RENENE.2023.119218.

73. A. Nybø, F. G. Nielsen, and M. Godvik, "Sensitivity of the Dynamic Response of a Multimegawatt Floating Wind Turbine to the Choice of Turbulence Model," *Wind Energy* 25, no. 6 (2022): 1013–1029, https://doi.org/10.1002/WE.2712.

74. A. Nybø, F. G. Nielsen, J. Reuder, M. J. Churchfield, and M. Godvik, "Evaluation of Different Wind Fields for the Investigation of the Dynamic Response of Offshore Wind Turbines," *Wind Energy* 23, no. 9 (2020): 1810–1830, https://doi.org/10.1002/WE.2518.

75. K. Shaler, J. Jonkman, P. Doubrawa, and N. Hamilton, "FAST. Farm Response to Varying Wind Inflow Techniques: Preprint". Tech. rep. NREL/CP-5000-72893, Jan. 2019. url: https://www.nrel.gov/docs/fy19osti/72893.pdf.

76. A. Wise and E. E. Bachynski, "Analysis of Wake Effects on Global Responses for a Floating Two-Turbine Case," *Journal of Physics: Conference Series* 1356, no. 1 (2019): 12004, https://doi.org/10.1088/1742-6596/1356/1/012004.

77. A. S. Wise and E. E. Bachynski, "Wake Meandering Effects on Floating Wind Turbines," *Wind Energy* 23, no. 5 (2020): 1266–1285, https://doi.org/10.1002/we.2485.

78. A. Sathe, J. Mann, T. K. Barlas, W. A. A. M. Bierbooms, and G. J. W. Van Bussel, "Atmospheric Stability and Its Influence on Wind Turbine Loads," in *TORQUE: The Science of Making Torque From Wind* (APA, 2012).

79. H. B. Hendriks and B. H. Bulder, "Fatigue Equivalent Load Cycle Method". Tech. rep. Petten: Energy Research Centre of the Netherlands (ECN), Apr. 1995, https://publicaties.ecn.nl/PdfFetch.aspx?nr=ECN-C%E2%80%9395-074.

80. M. C. Holtslag, W. A. A. M. Bierbooms, and G. J. W. Van Bussel, "Estimating Atmospheric Stability From Observations and Correcting Wind Shear Models Accordingly," *Journal of Physics: Conference Series* 555, no. 1 (2014): 012052, https://doi.org/10.1088/1742-6596/555/1/012052.

81. K. Thomsen "The Statistical Variation of Wind Turbine Fatigue Loads". In: IEA Joint Action. Wind Turbine Fatigue. Technical University of Denmark. Department of Fluid Mechanics, Oct. 2000, pp. 1–15, https://orbit.dtu.dk/en/publications/the-statistical-variation-of-windturbine-fatigue-loads-2.

82. Delft High Performance Computing Centre (DHPC) "DelftBlue Supercomputer (Phase 2)" 2024 https://www.tudelft.nl/dhpc/ark:/44463/DelftBluePhase2.

83. V. Martínez-Cagigal, "Custom Colormap" (2025), https://nl.mathworks.com/matlabcentral/fileexchange/69470-custom-colormap.

84. E. Cheynet, "Software-PolarPcolor". Tech. Rep. 2020, https://doi.org/10.5281/ZENODO.3774156.

Appendix A

This section provides the validation of the implementation of the Poisson equation solver in Algorithm 1. Two cases are considered for validation. First, a manufactured example was considered to solve a general Poisson equation. That is, to solve $\mathscr{L}(\phi) = f$, where f is typically called a source term. ϕ was chosen as $\phi = cos\left(\frac{x}{2}\right)sin(y)cos\left(\frac{z}{2}\right)$. Thus, it can be found that $\mathscr{L}(\phi) = -1.5\phi$. Note that ϕ is nonperiodic in the x- and z-directions. This was chosen to validate the mirror extension approach alongside the general solver validation. This example was solved using both the finite difference and the spectral methods to validate the implemented solver. The number of grid points was chosen as $N_x = N_y = N_z = 32$, and the domain size was chosen as $L_x = L_y = L_z = 2\pi$, centered around 0. Neumann boundary conditions were used for the x and z-directions while periodic boundary conditions were used for the y direction, in line with the characteristics of ϕ. The exact solution or, in this case, the chosen function ϕ is shown in Figure A1a, at $z = L_z / 2$.

The solution error of this first example, with the use of FDM, is shown in Figure A1b, and the solution error using the Fourier method is demonstrated in Figure A1c for the same location: the FDM employed matrix inversion, iterative, biconjugate gradient, or multigrid methods. In Figure A1b, it is observed that the error from the exact solution is acceptable, in the order of 10^{-3}, upon use of the matrix inversion method. Note that this error could have been further reduced by, for example, increasing the number of chosen grid points and/or using a higher order FDM, albeit at the cost of higher computational expense. Next, in Figure A1c, it can be seen that the solution error is in the order of machine precision, 10^{-16}. This is attributed to the fact that with the correct implementation, the chosen Poisson equation should be solved accurately in the Fourier method, given the continuous sine and cosine functions, despite the nonperiodicity. Thus, the implementation of the Poisson solver is validated using the manufactured example. Next, the solver was validated in terms of the divergence-correction algorithm in its entirety, in an unconstrained form of Algorithm 1. That is, to solve $\mathscr{L}(\phi) = f$ and $\nabla\phi$, with $f = \nabla \cdot \vec{\zeta}$, where $\vec{\zeta}$ is the original wind field and $\nabla\phi$ is the gradient of the scalar potential to be subtracted from the original wind field to obtain the divergence-free wind field (Equation (6)). The scalar potential ϕ was again found by solving Poisson's equation using the FDM and Fourier methods. Given that the wind field, $\vec{\zeta}$, was a 3-D wind field, the resulting $\nabla\phi$ is plotted in the three directions, in Figure A2. In Figure A2, the left plot in each subfigure shows the gradient of the scalar potential through a stream-wise line along 170-m altitude. The right plot in each subfigure shows the difference between the solution from the FDM and the Fourier method, in the entire domain. The FDM results are once again demonstrated by the use of matrix inversion. The results show that both methods provide a similar magnitude of the result and the trend. The difference in solutions as indicated in, for example, Figure A2a, is within $\pm$ 0.05 m/s and thus demonstrates the capability of the implemented Fourier method compared to the typically used FDM.

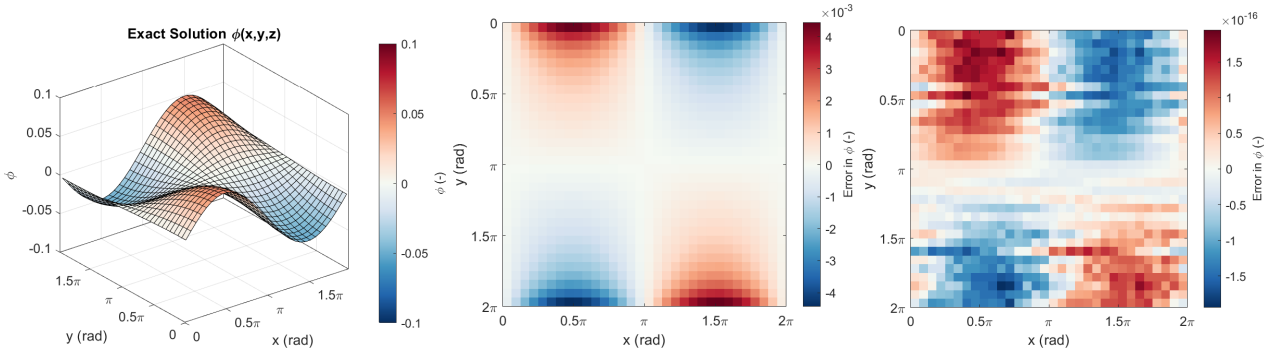

(a) Exact solution at a $z = L_z/2$. (b) Solution error using the finite-difference method. (c) Solution error using the FFT method.

FIGURE A1 | Solver validation on a manufactured example.

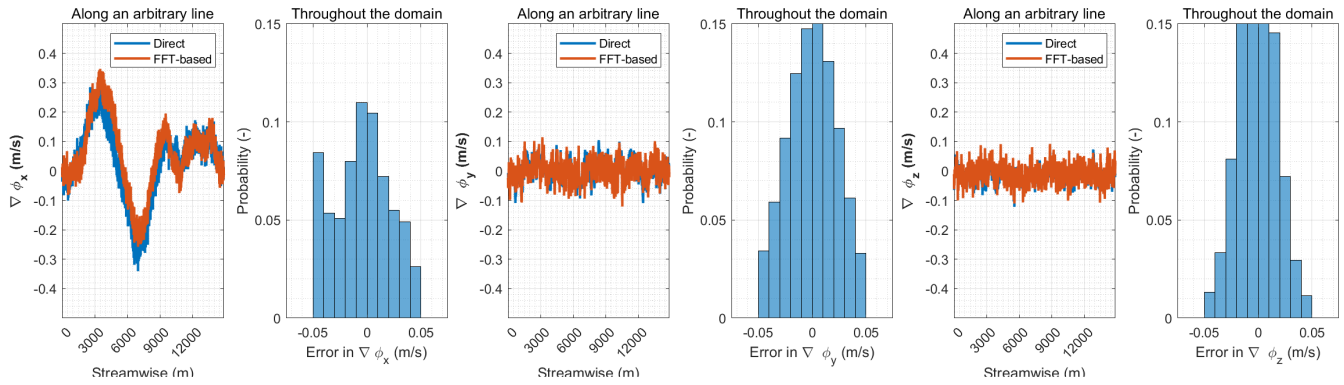

(a) For the $\nabla\phi$ in the x direction. (b) For the $\nabla\phi$ in the y direction. (c) For the $\nabla\phi$ in the z-direction.

FIGURE A2 | Solver validation on a wind field made divergence-free using the solver for the Helmholtz decomposition. The resulting $\nabla\phi$ is compared.

Appendix B

Unconstrained Algorithm-Based Divergence-Free Wind Field Characteristics

This section briefly compares the divergence-free wind field in contrast to the original wind field, upon using an unconstrained form of Algorithm 1. First, the order of reduction in divergence can be visualized from Figure B1a. The order of divergence was found to be 10^{-4}, thus, in one way, validating the implemented algorithm. Next, the instantaneous u component of wind speed is shown at an altitude of 170 m, which is the hub height of the IEA 22-MW wind turbine. Deviations from the original wind field were generally found to be within 0.5 m/s but sometimes larger up to 1 m/s. The resulting change in energy spectrum is shown in Figure B1c. Unlike the excellent match in energy spectrum in Figure 5a, here, a drop in energy spectrum is observed, which is also reported in literature [20, 69]. Lastly, the wind shear and the standard deviation along the altitude are shown for the u component. Once again, mean wind profiles are similar, but the unsteady profiles indicate changes of up to − 20%. Such discrepancies motivate the proposed constrained Algorithm 1 or the optimization approach proposed by the authors of [39].

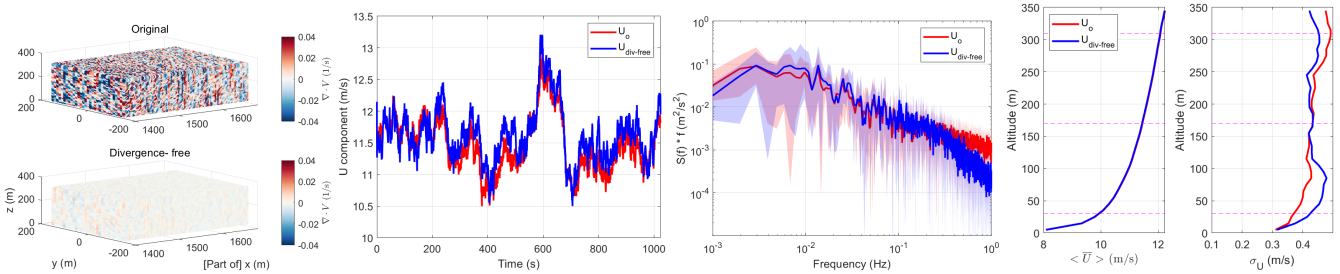

(a) Comparison of divergence before and after the correction.

(b) Comparison of instantaneous component u of wind field field.

(c) Comparison of u component energy spectra.

(d) Comparison of mean and standard deviation of wind field at different altitudes.

FIGURE B1 | An example of the changes in wind field upon use of the unconstrained algorithm to obtain the divergence-free wind field. Note the larger changes, for example, compared to Figure 4b.

Appendix C

Grid Sensitivity

In Appendix A, the developed Poisson solver for the Helmholtz–Hodge decomposition was validated. In this section, the robustness of the solver is assessed in terms of its sensitivity to changes in grid size. This is done using four different resolutions for synthetic wind field generation using the SHIW0 coherence model (Equation (3)) for the at-rated operating condition. The comprehensive study discussed in Section 3 and Section 4 utilized a grid spacing of 10 m in the lateral and vertical directions by using 35 cells in each direction. The grid sensitivity here is assessed by utilizing 25, 35, 45, and 55 cells in the lateral and vertical directions. This leads to Δy and Δz being 14, 10, 7.78, and 6.36 m, respectively. The stream-wise spacing (Δx) resulting from the chosen time step and the time–space conversion using Taylor's hypothesis is the same as that of the main study. Here, it is 2.875 m given the at-rated operation wind speed at hub height. With this setup, it can be noted that the sensitivity study inherently assesses the solver's robustness to different cell aspect ratios.

The results of the grid sensitivity study are shown in Figure C1. Firstly, the divergence throughout the domain is shown in Figure C1a by means of histograms. Here, the histograms are made with a bin-width coarser than in Figure 2 to allow for easier visualization given the multiple histograms. Nevertheless, it can be seen that the divergence correction is similar for the several grid sizes. Next, the important wind field statistics are presented, where the solid lines indicate the statistics of the original nonsolenoidal wind field and the dashed lines indicate the statistics of the corrected divergence-free wind field. The u and v component energy spectrum are shown in Figure C1b and Figure C1c, respectively. These are made by block-averaging for easier visualization of multiple cases. It can be observed once again that the different grid resolutions do not affect the solver's performance. Lastly, the wind speed and turbulence shear are shown in Figure C1d. The differences in mean wind shear between the grid resolutions are unremarkable, while there are differences in turbulence shear between the grid resolutions. The turbulence at hub height of 170 m is the same because a uniform scaling was enforced to ensure comparable wind turbine response in different wind fields. Differences at other altitudes are seen; however, these are attributed to the synthetic wind field generation in general. The solver can perform similarly regarding changes to the turbulence shear.

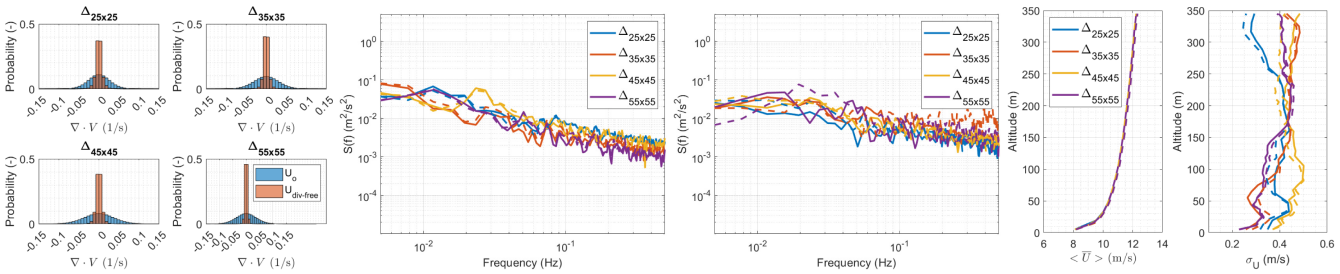

(a) Comparison of divergence before and after the correction.

(b) Comparison of u component energy spectra.

(c) Comparison of v component energy spectra.

(d) Comparison of mean and standard deviation of wind field at different altitudes.

FIGURE C1 | An example of the changes in wind field upon use of the algorithm to obtain the divergence-free wind field. A sensitivity of changes to the grid resolution is shown.

Appendix D

Visualization of the Impact of Differences in Turbulence Shear

In Section 4, the differences in the standard deviation of the loads between the original nonsolenoidal and the divergence-free wind fields were attributed mainly to the differences in wind field unsteadiness. These differences were manifested in the azimuthal dispersion of the rotor perceived velocity and are reflected in the below presented standard deviation of loads in each azimuthal bin (Figure D1 and Figure D2). The mean azimuthal variation was within ± 5% and thus not shown for brevity. Furthermore, here, a subset of results is shown for the SHIW0 coherence model-based wind field at different operating conditions. These plots were made using the open-source MATLAB functions [83, 84].

The azimuthal variation of σ_{F_x} (normal force) shown in Figure D1, and the σ_{F_y} (tangential force) shown in Figure D2 illustrates a noticeable general reduction in the load unsteadiness in the upper half of the rotor, in comparison to the unsteadiness in the original nonsolenoidal wind fields, especially for the below-rated operating conditions (Figure D1a and Figure D2a). As expected, the differences are higher for the below-rated operation condition, and lower for the at-rated and above-rated operating conditions.

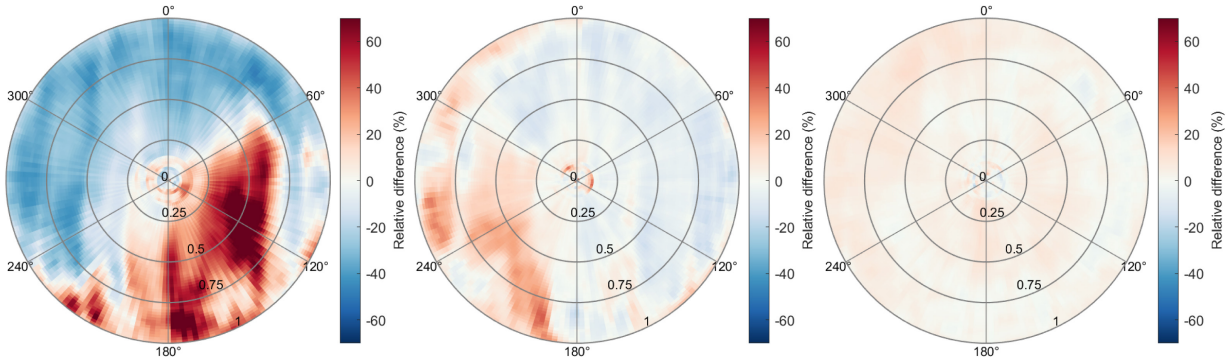

(a) Below rated operating condition (b) At rated operating condition (c) Above rated operating condition

FIGURE D1 | Relative differences in the azimuthal dispersion of axial force (σ_{F_x}) in the SHIW0 coherence model-based divergence-free wind field, in comparison to the original nonsolenoidal wind field, at different operating conditions.

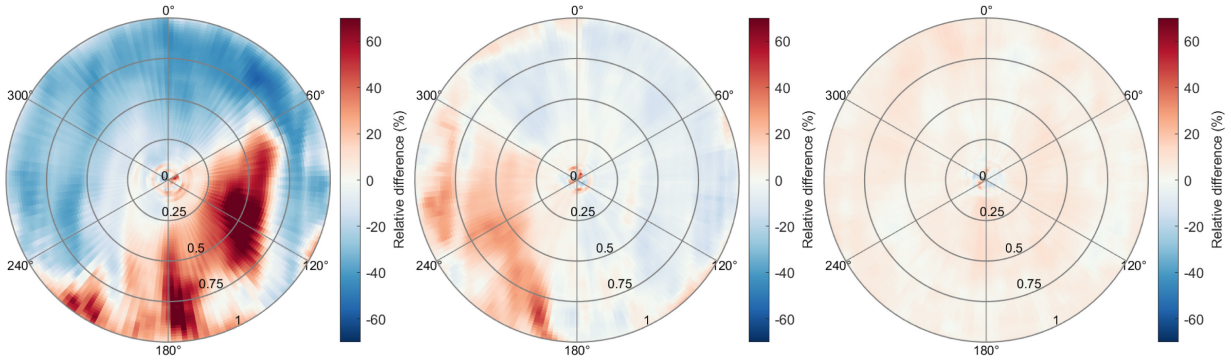

(a) Below rated operating condition (b) At rated operating condition (c) Aboverated operating condition

FIGURE D2 | Relative differences in the azimuthal dispersion of tangential (σ_{F_y}) force in the SHIW0 coherence model-based divergence-free wind field, in comparison to the original nonsolenoidal wind field, at different operating conditions.